Chapter 7
Control Design for Rotor Suspension

This chapter presents the design of the AMB rotor levitation controllers for the compressor test rig described in Chap. 4. First of all, we discuss in detail the different standards that have been developed for machines with AMBs. These standards are frequently referred to by both the compressor manufacturers and the end-users during the design, manufacturing and commissioning of AMB-supported machines. The general API standards for axial and centrifugal compressors were presented earlier in Chap. 2. Here we review the available standards that specifically target AMB-supported compressors and other rotating machines. The requirements and recommendations for new machines that are defined in these standards will be followed during the design of the AMB levitation controllers throughout this chapter.

Next, the derivation of the mathematical model describing the lateral and axial dynamics of the rotor/AMB system is presented. The finite-element approach discussed in Chap. 2 is combined with a modal reduction method in order to obtain an accurate reduced-order model of the rotor radial dynamics. The AMB actuator force equation and the dynamics of the electronic components in the control loop, such as the current amplifiers and the sensors, are also included in the final model. In the axial direction, the dynamic capabilities of the thrust AMB are susceptible to the eddy current losses and the back-EMF effect induced by the journal motion. Therefore, linearized approximations of these inefficiencies are also discussed.

Finally, the rotor levitation controllers are designed and implemented for the radial and thrust AMBs. The controllers presented in this chapter are designed to satisfy the API and ISO standards for new compressors with AMB supports. In the lateral direction, an LQG controller is designed to minimize the rotor vibrations caused by the rotor unbalance forces. For the thrust AMB, an H_∞ controller is synthesized to maximized the tracking performance of the impeller position. Accurate control of the rotor axial position is required for the success of the surge control strategy proposed in this book. In all cases, the controllers are implemented on the test rig, and experimental measurements are presented to validate the modeling and the characteristics of the theoretical closed-loop system.

7.1 Specifications for Machines with AMBs

Swanson et al. presented in [111] a discussion on the published rotor-dynamic standards and design recommendations available for machines with AMB supports. Same as in traditional rolling element and fluid-film bearings, the purpose of an AMB support is to limit the rotor vibration caused by the presence of external destabilizing forces. Therefore, it is expected that the basic rotor-dynamic specifications for machines supported on both AMBs and passive bearings focus on essentially the same concerns, which include the stability margin and unbalance response of the rotor/bearing system. The rotor-dynamic specifications developed by the American Petroleum Institute (API) for compressors were discussed in detail in Chap. 2, and large segments of these standards are directly applicable for machines with AMBs. However, there are some requirements in the API standards which were developed specifically based on the experiences with rolling element and fluid-film bearings. These requirements are largely considered to be inadequate for AMB applications [111]. For example, the API rotor vibration limit for compressors is given as the smallest of $\sqrt{12,000/N}$ mil and 1 mil, where N is the rotor speed in rpm. This is generally a very small fraction of the clearance available in AMB systems, and a more efficient and robust magnetic support system could be designed by relaxing the vibration requirement in machines with magnetic bearings.

The API 617 Annex 4F, *Application Considerations for Active Magnetic Bearings*, was the initial attempt by the API for accommodating the unique properties of the AMBs in the standards for expander-compressors. This addition to the API 617 standard was intended to acknowledge the advances made in the non-contact bearing technologies and to expand the existing requirements for API compliant machines. An important contribution of this informative section on active magnetic bearings is the increase in the maximum allowable rotor displacement relative to the auxiliary bearing center to 30 % of the minimum clearance. This provided a more realistic design requirement for AMB manufacturers in terms of maximum allowable rotor vibration level. New versions of the API 617 standard are expected to include additional requirements on the forced response and stability margin analyses specifically designed for the API compliant AMB-supported compressors.

The International Organization of Standardization also published a set of standards for AMB-supported machines. The ISO 14839 standards were developed to complement the requirements on the unbalance response and stability margin analyses as given in the various ISO standards for rotating machines. Differently from the API standards, which are defined to be strict acceptance criteria employed to evaluate the different machines in the refinery service, the ISO standards were presented as design recommendations for acceptable machines [111]. The ISO 14839 standards for rotating machines with AMBs categorize the rotor-dynamic systems based on the observed vibration level and stability margin.

Fig. 7.1 Rotor orbit as measured by ISO
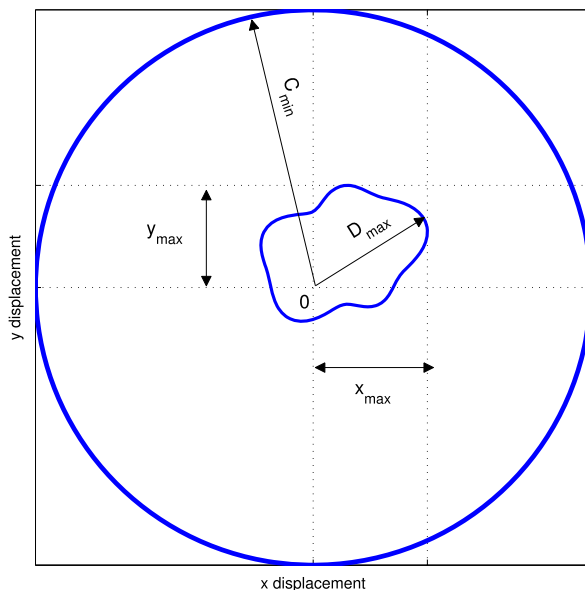
7.1.1 Vibration Level

The standard for evaluating the vibration level of AMB systems is defined in ISO 14839-2 *Mechanical Vibration—Vibration of Rotating Machinery Equipped with Active Magnetic Bearings—Part 2: Evaluation of Vibration* [66]. This standard defines the maximum rotor vibration levels for AMB-supported machines, and it is developed to work in junction with the ISO 10814 [64] to regulate the forced response characteristics of acceptable machines. The second part of the ISO 14839 also describes the required equipment configuration and testing procedure for evaluating the forced response.

Differently from traditional passive bearings, the rotor vibration level in the forced response of AMB systems is measured relative to the center of the component with the minimum clearance $C_{\min}$, as shown in Fig. 7.1. In most AMB systems, this corresponds to the center of the auxiliary bearing. The ISO standard 14839-2 defines the zones in the following manner based on the observed vibration level.

Zone A: Machines with vibration level normally expected for newly commissioned equipments. The peak rotor displacement for a machine in this zone is below 30 % of the minimum clearance $C_{\min}$.

Zone B: Machines with vibration level that is normally considered acceptable for unrestricted long-term operation. The peak rotor displacement for a machine in this zone is between 30 % and 40 % of the minimum clearance $C_{\min}$.

Zone C: Machines with vibration level that is normally considered unacceptable for long-term operation. Limited time operation of the machine is generally allowed

until remedial actions are taken in the next suitable opportunity. The peak rotor displacement for a machine in this zone is between 40 % and 50 % of the minimum clearance C_{min}.

Zone D: Machines with vibration level that are considered to be sufficiently severe to damage the equipment. The peak rotor displacement for a machine in this zone is above 50 % of the minimum clearance C_{min}.

The rotor-dynamic requirements on the amplification factors and separation margins corresponding to the critical speeds of the AMB system are the same as in the case of traditional passive bearings. For more information on these requirements, please refer to Chap. 2.

7.1.2 Stability Margin

The standard for evaluating the stability margin of AMB systems is defined in ISO 14839-3 *Mechanical Vibration—Vibration of Rotating Machinery Equipped with Active Magnetic Bearings—Part 3: Evaluation of Stability Margin* [67]. Differently from the other standards developed for AMB-supported machines, ISO 14839 introduces a new method to evaluate the stability margin of the AMB system. The approach described in ISO 14839-3 is related to the phase margin and gain margin concepts presented in Chap. 6. The peak magnitude value of the closed-loop AMB sensitivity function is inversely proportional to the gain margin of the system, as shown in [67]. Therefore, a smaller peak in the sensitivity function corresponds to a larger gain margin of the AMB system, and thus a larger stability margin.

The perturbation and measurement points specified in the ISO 14839-3 standard for obtaining the sensitivity function $S(s)$ is shown in Fig. 7.2 for a single AMB control axis. The input signal $E(s)$ is the injection point of the excitation signal. The ISO 14839-3 standard defines four zones based on the peak magnitude of the sensitivity function.

Zone A: Machines with sensitivity functions normally expected for newly commissioned equipments. The peak magnitude of the sensitivity function for a machine in this zone is below 3 (9.5 dB).

Zone B: Machines with sensitivity functions that are normally considered acceptable for unrestricted long-term operation. The peak magnitude of the sensitivity function for a machine in this zone is between 3 (9.5 dB) and 4 (12 dB).

Zone C: Machines with sensitivity functions that are normally considered unacceptable for long-term operation. Limited time operation of the machine is generally allowed until remedial actions are taken in the next suitable opportunity. The peak magnitude of the sensitivity function for a machine in this zone is between 4 (12 dB) and 5 (14 dB).

Zone D: Machines with sensitivity functions that are considered to be sufficiently severe to damage the equipment. The peak magnitude of the sensitivity function for a machine in this zone is above 5 (14 dB).
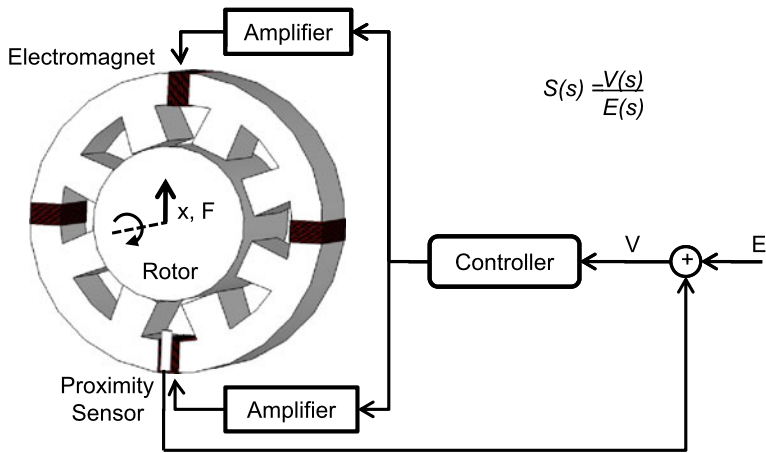
Fig. 7.2 Measurement points for the sensitivity function

Table 7.1 Zone limit criteria as recommended by ISO 14839 [65–67]

Zone Limit	Max. Displacement	Peak Sensitivity
A/B	$<0.3C_{min}$	<3 (9.5 dB)
B/C	$<0.4C_{min}$	<4 (12 dB)
C/D	$<0.5C_{min}$	<5 (14 dB)

Because the magnitudes of the gyroscopic forces acting on the rotor change within the operating speeds range, the closed-loop sensitivity function will vary for different operating conditions of an AMB-supported machine. Therefore, the peak magnitude of the sensitivity function is required to be checked for the machine at zero speed and the maximum continuous operating speed.

The stability margin criteria defined in ISO 14839-3 result in a simple test to identify the AMB rotor suspension systems that are reasonably robust to gain and phase uncertainties in the control loop. These uncertainties are introduced, for example, by the unmodeled time delays, the sensor and amplifier calibration error, and even the modeling error in the open-loop actuator gains. However, as noted in [111], phase and gain margins by themselves cannot guarantee system robustness to a more general group of uncertainties that are common in AMB systems. Uncertainties in the critical speed and the cross-coupling stiffness, which were found in [83] to rapidly drive the AMB system to instability, require more advanced robustness conditions to guarantee the stability of the rotor levitation system. Therefore, the stability margin test described in ISO 14839-3 should be accompanied by more comprehensive robustness tests in control theory when possible. A summary of the vibration and stability margin criteria for each of the ISO zones is presented in Table 7.1.
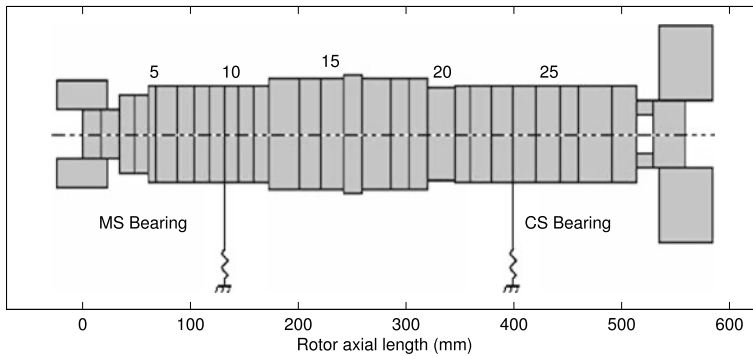
Fig. 7.3   Mesh of the rotor for finite-element modeling

7.2 Modeling of the AMB Suspension System

An AMB-supported compressor test rig, commissioned for the study of active surge control, was first introduced in Chap. 4. In this section, we present the derivation of the mathematical model describing the dynamics of the AMB system in this compressor test rig. The main components of the AMB levitation system is the rotor, the AMB actuator, the power amplifier, and the displacement sensor electronics. In this section, each of these components is modeled separately following the results presented in Chaps. 2, 3 and 4. Additionally, the losses in the magnetic bearings affecting the dynamics the closed-loop rotor levitation system are also discussed, and approximated models are proposed to capture the resulting loss in the bearing performance.

7.2.1 Rotor Lateral Dynamics

In this section we derive the system of equations describing the lateral dynamics of the compressor rotor. The finite-element methods (FEM) introduced in Chap. 2 is employed to approximate the distributed parameter dynamics of the rotor into a finite dimensional model. The tuned mesh of the compressor rotor for FEM modeling is shown in Fig. 7.3, where the shaft is sectioned into small beam elements. Additional rotor disks, impellers and bearing journals are added as mass/inertia disks at the elements' node points. The input of the resulting FEM model is the forces at the bearing location nodes 10 and 24, and the output is the rotor lateral displacements at the sensor location nodes 9 and 25.

   We notice that the rotor geometry in Fig. 7.3 differs slightly from the actual rotor shape presented in Chap. 4. This is because the FEM model has been corrected based on the results from the experimental ring test. As commonly done in rotating machinery, the rotor resonance frequencies are measured in the ring test by suspending the rotor on piano wires and measuring the rotor vibration to a hammer

impact. Accurate frequency response data of the rotor vibration are obtained by using accelerometers installed along the rotor length. The rotor geometry presented in this section corresponds to the validated model, where the rotor properties has been tuned to match the modeled resonance frequencies to the measured values.

The general structure of the vector differential equation for a cylindrical undamped rotor with mass matrix M, gyroscopic matrix G and stiffness matrix K is found from the FEM formulation as,

$$
\begin{bmatrix} M & 0 \\ 0 & M \end{bmatrix} \begin{bmatrix} \ddot{q}_x \\ \ddot{q}_y \end{bmatrix} + \omega \begin{bmatrix} 0 & G \\ G & 0 \end{bmatrix} \begin{bmatrix} \dot{q}_x \\ \dot{q}_y \end{bmatrix} + \begin{bmatrix} K & 0 \\ 0 & K \end{bmatrix} \begin{bmatrix} q_x \\ q_y \end{bmatrix} = \begin{bmatrix} F & 0 \\ 0 & F \end{bmatrix} \begin{bmatrix} u_x \\ u_y \end{bmatrix}. \quad (7.1)
$$

The state vector q_x describes the rotor dynamics in the x-direction, and the vector q_y is composed of the rotor states in the y-direction. Matrix F describes how the decoupled external forces in the x-direction u_x and the y-direction u_y affect the lateral dynamics of the rotor. The differential equation in Eq. (7.1) shows that the rotor dynamics in the x- and y-directions are only coupled by the gyroscopic effects, which is dependent on the rotor speed ω.

The state vector in Eq. (7.1) for a rotor model with n-elements has a total number of $4(n+1)$ states. These states correspond to the two lateral and two angular degrees of freedom assigned to each node point. Therefore, the total number of states increases fast as the number of node points increases for rotors with complex geometries. A dynamic model with a large state vector is computationally intensive to simulate, and can lead to numerical problems during the design of the AMB rotor suspension controller. A common method for reducing the size of the state vector in the rotor model is the modal reduction approach. In this method, the system equation in Eq. (7.1) is transformed into the modal coordinates, and the states corresponding to irrelevant high-frequency modes are truncated. The method for truncating the high-frequency dynamics is demonstrated below. In general, the states dominating the dynamics of the rotor correspond to the resonance modes in the low frequency range.

The transformation matrix taking the rotor state vector from the physical coordinates to the modal coordinates is obtained by solving the generalized eigenvalue problem,

$$
K\Phi = M\Phi\Lambda^2. \quad (7.2)
$$

The diagonal matrix Λ is composed of the rotor resonance mode frequencies, and the columns of the nonsingular matrix Φ are the vector mode shapes corresponding to the undamped rotor. Here, the matrix Φ is normalized such that

$$
\Phi^T M \Phi = I, \quad (7.3)
$$

and

$$
\Phi^T K \Phi = \Lambda^2. \quad (7.4)
$$

Define the new state vectors ξ_x and ξ_y in the modal coordinates such that

$$
\Phi\xi_x = q_x, \quad (7.5)
$$

and

$$\Phi \xi_y = q_y. \tag{7.6}$$

The newly defined states are substituted into Eq. (7.1), and the resulting system of equations is multiplied to the left by Φ^T. The differential equations in the modal coordinates describing the lateral dynamics of the undamped rotor are found to be

$$\Phi^T M \Phi \ddot{\xi}_x + \omega \Phi^T G \Phi \dot{\xi}_y + \Phi^T K \Phi \xi_x = \Phi^T F u_x, \tag{7.7a}$$

$$\Phi^T M \Phi \ddot{\xi}_y - \omega \Phi^T G \Phi \dot{\xi}_x + \Phi^T K \Phi \xi_y = \Phi^T F u_y. \tag{7.7b}$$

Finally, substituting the equalities in Eqs. (7.3) and (7.4) into the above system of equations, we obtain

$$\ddot{\xi}_x + \omega G_m \dot{\xi}_y + \Lambda^2 \xi_x = F_m u_x, \tag{7.8a}$$

$$\ddot{\xi}_y - \omega G_m \dot{\xi}_x + \Lambda^2 \xi_y = F_m u_y. \tag{7.8b}$$

Consider the lateral dynamics of the rotor in the x-axis in Eq. (7.8a). Assuming momentarily that there is no gyroscopic moment acting on the rotor ($\omega = 0$), we rewrite the dynamic equation in Eq. (7.8a) in the standard state space form as,

$$\begin{bmatrix} \dot{\xi}_x \\ \ddot{\xi}_x \end{bmatrix} = A_x \begin{bmatrix} \xi_x \\ \dot{\xi}_x \end{bmatrix} + B_x u_x. \tag{7.9}$$

The state space matrices of the above system are given by

$$A_x = \begin{bmatrix} 0 & I \\ -\Lambda^2 & 2\zeta\Lambda \end{bmatrix}, \tag{7.10a}$$

$$B_x = \begin{bmatrix} 0 \\ F_m \end{bmatrix}. \tag{7.10b}$$

An empirical modal damping coefficient ζ is added to the model, which stabilizes the modes of the rotor lateral dynamics. For the rotor in the compressor test rig, a reasonable modal damping of 0.1 % ($\zeta = 0.001$) was selected. Following the same process as demonstrated above, we can also derive the state space equation for the y-axis. The resulting state space matrices corresponding to the y-axis dynamics are the same as in the x-direction in Eq. (7.9). Finally, for $\omega \neq 0$, the x- and y-axes are coupled by the gyroscopic effect. The state space equation for the complete rotor lateral dynamics with gyroscopic effects is found to be

$$\dot{x} = \begin{bmatrix} A_x & -\omega G_m \\ \omega G_m & A_x \end{bmatrix} x + \begin{bmatrix} B_x & 0 \\ 0 & B_x \end{bmatrix} u. \tag{7.11}$$

The algorithm described in this section for obtaining the reduced-order state space model of the free–free rotor was implemented in the computer program *modal*. This
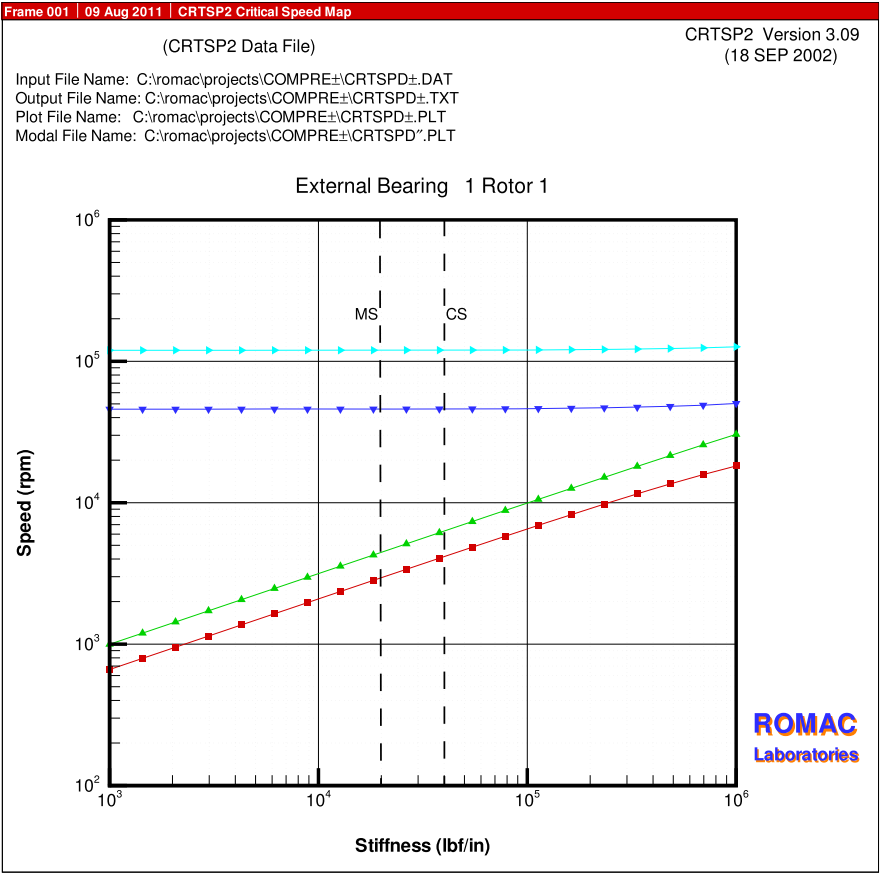
Fig. 7.4 Rotor critical speed map

tool, available in the ROMAC software library, was employed in this study to find the numerical values of the state space matrices A_x, B_x and G_m in the final rotor model.

The eigenvalues of the state matrix in Eq. (7.11) give the frequencies of the rotor resonance modes. These modes are shown in the critical speed map in Fig. 7.4. The plot shows the change in the frequency of the rotor modes as a function of the bearing support stiffness. The first two critical speeds Nc1 and Nc2 correspond to the free–free rigid body modes of the rotor. These modes are also generally called the parallel mode and the conical mode, respectively. The next two critical speeds in Fig. 7.4 are Nc3 and Nc4, which correspond to the first and second free–free bending modes. The critical speed map in Fig. 7.4 also shows the predicted closed-loop stiffness of the radial AMBs at the motor side and the compressor side. As discussed in Chap. 3, these values are estimated to be three times the open-loop stiffness K_x of the corresponding AMB.
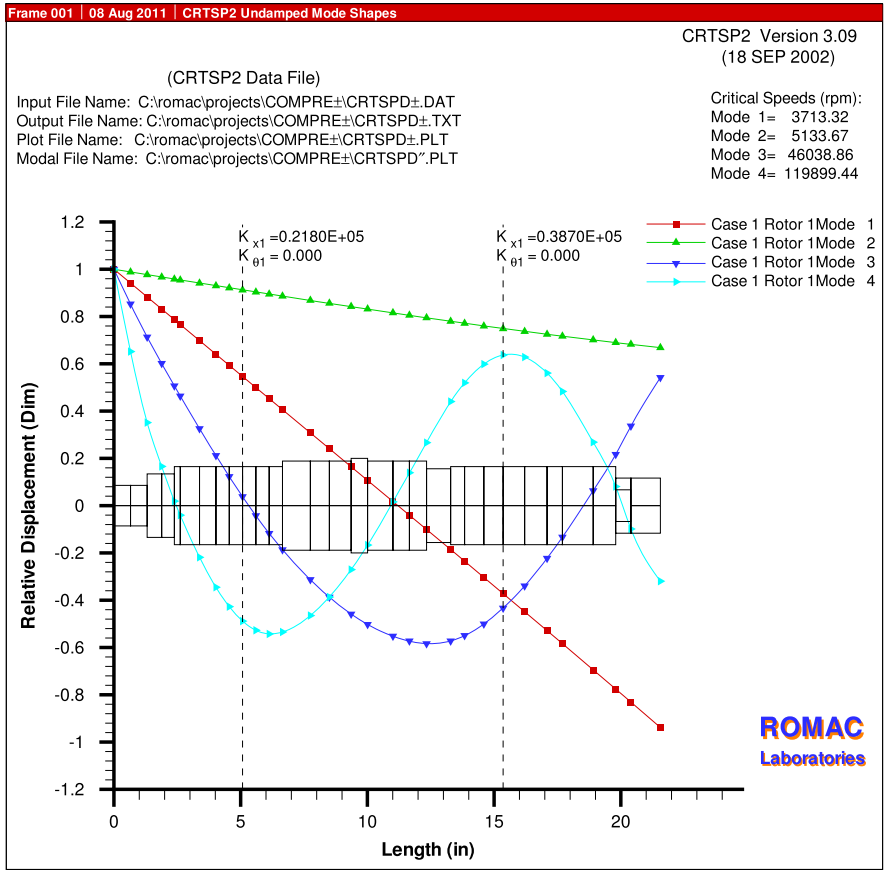
Fig. 7.5 Rotor bending mode shapes with approximated support stiffness

The critical speeds and the mode shapes corresponding to the first four rotor modes are shown in Fig. 7.5. The stiffness of the support bearings in this analysis was taken to be the estimated closed-loop stiffness of the AMBs. The frequencies of mode number one (Nc1) and mode number two (Nc2) are below the maximum design speed of the compressor. The mode shapes show that Nc1 and Nc2 correspond to the parallel and conical modes, which govern the rigid body dynamics of the rotor. The first bending mode at the current support stiffness is mode number three (Nc3), and the estimated separation margin for this mode is over 100 %. Therefore, we can consider the lateral dynamics of the compressor rotor to be rigid.

Although the above analysis shows that the rotor lateral dynamics are dominated by the rigid body modes, it is a good practice in AMB systems for the final rotor model to include all the modes that fall within the AMB controller bandwidth. Differently from passive bearings that normally only excite the rotor
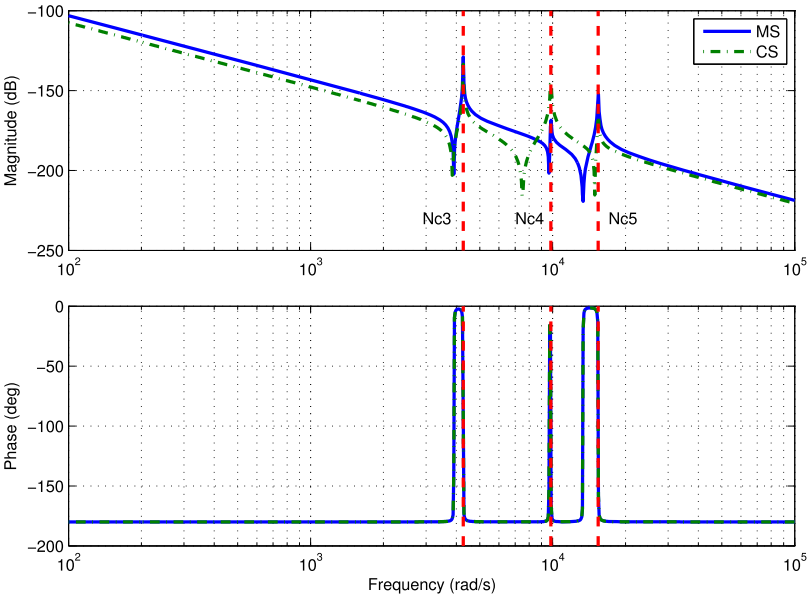
Fig. 7.6 Bode plots of the lateral rotor model at the motor side (MS) and compressor side (CS)

Table 7.2 Rotor mode frequency and damping

Critical Speed	Frequency (rad/s)	Damping Factor
Parallel (Nc1)	0	0
Conical (Nc2)	0	0
First bending (Nc3)	4,271.8	0.001
Second bending (Nc4)	9,829.5	0.001
Third bending (Nc5)	15,422	0.001

at the synchronous frequency (equal to the rotating speed), the controller in an AMB system can potentially introduce considerable energy in a broad range of frequencies. Therefore, it is important that the design of the AMB rotor suspension controller includes the information of any critical speed located within the control bandwidth. In the compressor test rig, the maximum bandwidth of the controller is limited by the hardware and software of the digital implementation to 15.7×10^3 rad/s (2.5 kHz). Therefore, the final state space model of the rotor lateral dynamics is reduced to include the first five free–free modes. The Bode plots of the modeled rotor lateral dynamics are shown in Fig. 7.6. Also, the frequencies and damping coefficients of the free–free rotor modes are listed in Table 7.2.

7.2.2 Rotor Axial Dynamics

Because of the general geometry of rotors, the resonance frequencies of the axial modes are much higher than those of the lateral modes. Therefore, the rotor is here considered to be rigid in the axial direction, and its dynamics are modeled as a free solid mass with a given inertia. Additionally, the thrust AMB is hardly affected by the non-collocation of the sensor and the AMB actuator, and the displacements at the sensor and bearing locations are considered to be identical. The differential equation for the axial dynamics of the unsupported rotor is given by

$$m_r \ddot{z} = u_z, \tag{7.12}$$

where z is the axial rotor displacement, m_r is the total mass of the rotor, and u_z is the axial external force acting on the rotor. The state space equation of the rotor in the axial direction is,

$$\begin{bmatrix} \dot{z} \\ \ddot{z} \end{bmatrix} = \begin{bmatrix} 0 & 1 \\ 0 & 0 \end{bmatrix} \begin{bmatrix} z \\ \dot{z} \end{bmatrix} + \begin{bmatrix} 0 \\ \frac{1}{m_r} \end{bmatrix} u_z. \tag{7.13}$$

This state space system has two poles at the origin, corresponding to the rigid body dynamics of the rotor.
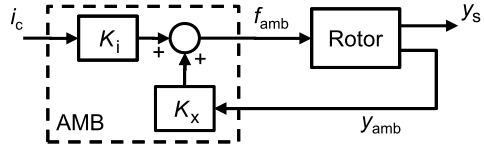
7.2.3 AMB Actuator

The linearized force equation derived in Eq. (3.30) is employed for the model of the magnetic bearing actuators in both the radial and the axial directions. Recall that the combined force applied by the opposite coils of an AMB actuator in the direction of a control axis f_{amb} is a function of the control current i_c and the rotor displacement at the location of the bearing y_{amb},

$$f_{amb} = K_i i_c + K_x y_{amb}. \tag{7.14}$$

The open-loop stiffness K_x and the open-loop current gain K_i of the compressor AMBs were given in Table 4.2. The block diagram illustrating the connection between the AMB force equation in Eq. (7.14) and the free–free rotor model is presented in Fig. 7.7. It is important to note that, because of the non-collocation of the sensor and the AMB actuator, the rotor displacements at the sensor and bearing locations may not be the same. For the compressor test rig, the force equations of the AMB actuators use the rotor lateral displacements at the node points 10 and 24 in the finite-element model, while the displacement sensors measure the rotor motion at the node points 9 and 25. On the other hand, for the case of the thrust AMB, the axial displacements are considered to be the same for the sensor and actuator locations.

Fig. 7.7 Rotor/AMB
connection

7.2.4 Power Amplifiers, Sensor Electronics and Time Delays

The coil of the AMB actuator forms a resistance–inductance (RL) circuit that is powered by the power amplifier providing the control current i_c. As mentioned in Chap. 3, this RL circuit limits the slew rate of the control current, and it is generally modeled together with the internal dynamics of the power amplifier as a simple low pass filter at the input of the AMB force equation. The time constant of this low pass filter depends on a series of factors such as the coil inductance, the coil resistance, the power source voltage and the tuning of the power amplifier. A common approach is to obtain the time constant empirically. The time constant for both the radial and the axial AMB systems in the compressor test rig was identified in Chap. 4 to be $\tau_a = 0.2$ ms.

The input to the power amplifier is the command voltage signal from the implemented rotor levitation controller. This signal is converted into the control current to the AMB force equation, and the conversion ratio is given by the amplifier gain. For the compressor test rig, the amplifier gain is calibrated to be $K_a = 1.5$ A/V in both the radial and the axial directions. In our model of the AMB system, the amplifier gain information is included in the amplifier/RL-circuit model at the input of the AMB force equation. Therefore, the so-called "amplifier model" is a single-order low pass filter with a DC-gain of K_a and a time constant of τ_a.

The output of the rotor model that is observed in the AMB system is the displacements at the sensor measurement points. These displacements are captured by the feedback sensors and converted into equivalent voltage signals. The bandwidth of the sensor measurements is commonly limited by the signal conditioning circuits, which converts the original sensor output to an analog voltage signal that is readable by the digital controller. For AMB systems with digital controllers, the bandwidth of the sensor measurement signal must be lower than the Nyquist frequency corresponding to the controller sampling time. This limitation in the bandwidth is needed in order to prevent aliasing noise in the feedback system. In the compressor test rig, the dynamics of the radial sensor circuits are modeled as low pass filters with a time constant of $\tau_s = 0.07$ ms and a gain of $K_{s,r} = 39.37$ V/mm. The sensor gain corresponds to an output voltage range of ± 10 V representing the range of the rotor radial displacement. In the case of the thrust AMB, the sensor calibration resulted in a gain of $K_{s,t} = 27.56$ V/mm.

Finally, a time delay is included in the system model to represent the sampling and computational delays added by the digital components in the control loop. A reasonable time delay for mechatronic applications such as AMBs is 1.5 times the sampling time of the digital equipment. The sampling frequency of the digital AMB rotor support controller in the compressor test rig is
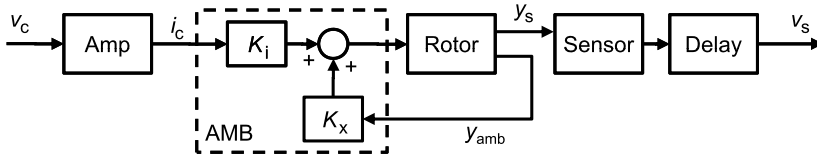
**Fig. 7.8** Block diagram of the total AMB system

3.14×10^4 rad/s (5 kHz). In the mathematical model of the AMB system, a second order Pade approximation of the delay function was used. The block diagram of the total AMB system is shown in Fig. 7.8. The input to the AMB system is the control voltage signal v_c from the controller implementation to the power amplifiers. The output signal of the AMB system is the voltage signal v_s from the rotor displacement sensor back to the levitation controller. The complete AMB system state space model in the radial direction has a total of 24 states.

7.2.5 Losses Due to Eddy Current in the Thrust AMB

As described in Chap. 3, the exposure of the conductive material in the AMB actuator and rotor to an oscillating magnetic flux induces the formation of eddy current loops. The losses due to the eddy current in most heteropolar radial AMBs can be significantly reduced by breaking the induced loops through rotor and stator lamination. Therefore, the eddy current losses has minimal effect on the dynamics of these radial AMBs. For thrust AMBs on the other hand, laminations of the stator and thrust disk are not practical with the available technology. Therefore, the eddy losses are more important for the solid target and actuators in the axial direction, and these losses affect the high-frequency dynamics of the thrust AMB system by significantly reducing the closed-loop bandwidth [76].

The authors of [124, 125] presented a method for modeling the performance limitation of the AMB actuators due to the eddy current losses. They introduced the concept of effective reluctance, which is a frequency dependent value that captures the effect of the eddy loop in the iron core. The simplified model of the eddy losses in the thrust AMB system, together with the back-EMF effect induced by the journal motion, are illustrated in Fig. 7.9. The time constant τ_a comes from the power amplifier model in Sect. 7.2.4. The constant R^0 is the static value of the effective reluctance, and c is the coefficient of the half order term for the total reluctance of the non-laminated actuator. The effects of the eddy looses and the back-EMF are added to the model of the thrust bearing in the compressor test rig. The fractional order system model of the eddy losses is approximated with a fourth order LTI transfer function, which was fitted from the frequency response of the original eddy loss model.

Fig. 7.9 Block diagram of the thrust AMB actuator/rotor
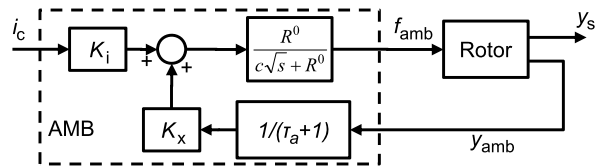
7.3 Control of Rotor Lateral Dynamics

The design of a rotor suspension controller is presented in this section, based on the lateral dynamics of the AMB system modeled in Sect. 7.2. The linear quadratic gaussian (LQG) method is proposed here for the design of the rotor radial support controller. This MIMO optimal-control method is preferred in this case over the PID controllers because of its capability to integrate multiple input and output of the plant to find the best control solution. While PID controllers are manually tuned channel by channel, the LQG algorithm takes the MIMO equations of the plant and automatically computes the optimal solution for a given objective function. Additionally, the LQG design process is generally considered to be simpler than the more advanced H_∞ and μ-synthesis control methods. This allows us to find multiple optimal LQG controllers in a short period of time, and to rapidly compare how different parameters of the optimization problem affect the performance of the final solution.

7.3.1 Linear Quadratic Gaussian (LQG) Controller

The linear quadratic regulators (LQR) is one of the most common optimal-control schemes for linear time-invariant systems, and a detailed discussion of the theory was presented in Chap. 6. Assume that we are given the following state space representation of an LTI system:

$$\dot{x}(t) = Ax(t) + Bu(t), \tag{7.15a}$$

$$x(t_0) = x_0, \tag{7.15b}$$

where x is the state vector, (A, B) is a controllable pair of state and input matrices, and x_0 is the initial condition of the states at time t_0. Then, the objective of the LQR design problem is to find the state-feedback control input $u(t)$ defined within $[t_0, T]$, which minimizes the quadratic cost function J_{LQR},

$$J_{\text{LQR}} = \int_{t_0}^{T} \left(x^\mathsf{T} Q x + u^\mathsf{T} R u \right) \mathrm{d}t. \tag{7.16}$$

The positive semidefinite matrix Q is the weight on the system states, and the positive definite matrix R is the weight on the control input. Therefore, the LQR cost function penalizes the variation of the system state from the origin and the control effort by the stabilizing controller. For the special case of T approaching infinity,

the optimal solution for the LQR problem may be found by solving the associated Algebraic Riccati Equation (ARE),

$$A^{\mathrm{T}}S + SA - SBRB^{\mathrm{T}}S + Q = 0. \tag{7.17}$$

In this case, a constant state-feedback gain matrix K is found to be

$$K = -R^{-1}B^{\mathrm{T}}S, \tag{7.18}$$

and the optimal-control input becomes

$$u(t) = Kx(t). \tag{7.19}$$

For more information on LQR control, please refer to Chap. 6.

In many physical systems the state measurements are not available for feedback to the controller. This is also true for AMB suspension systems, where the number of available sensors for control measurement is limited by the constraints in cost and space. For example, in the case of the compressor test rig presented in Chap. 4, we have the rotor displacement measurements at only five different locations along the spindle. These measure the rotor displacements in the directions of the two control axes for each radial bearing, and the axial rotor displacement for the thrust AMB control. In order to account for the limited number of feedback sensor measurements and the noise added in the input and output channels, a Gaussian observer is commonly coupled with the LQR controller in order to form an output feedback optimal controller. This new version of the linear quadratic regulator is commonly known as the linear quadratic gaussian (LQG) control.

Consider the state space equations of a dynamic system with input and output noises,

$$\dot{x}(t) = Ax(t) + Bu(t) + w, \tag{7.20a}$$

$$y(t) = Cx(t) + Du(t) + v, \tag{7.20b}$$

where C and D are the output matrices. The external input, w and v, is the state and the measurement noise, which are assumed to be Gaussian white noise with the covariance matrix

$$W_{\mathrm{n}} = E\left\{ \begin{bmatrix} w \\ v \end{bmatrix} \begin{bmatrix} w^{\mathrm{T}} & v^{\mathrm{T}} \end{bmatrix} \right\}, \tag{7.21}$$

where E stands for the expected value. The objective of the LQG design problem is once again to find an output feedback controller $K_{\mathrm{LQG}}(s)$, which minimizes the quadratic cost function J_{LQG},

$$J_{\mathrm{LQG}} = E\left\{ \lim_{T \to \infty} \int_0^T \left(x^{\mathrm{T}}Qx + u^{\mathrm{T}}Ru \right) \mathrm{d}t \right\}. \tag{7.22}$$

The resulting LQG regulator is a combination of an optimal LQR state-feedback controller and an optimal Gaussian observer that estimates the system states for the

Fig. 7.10 LQG controller structure
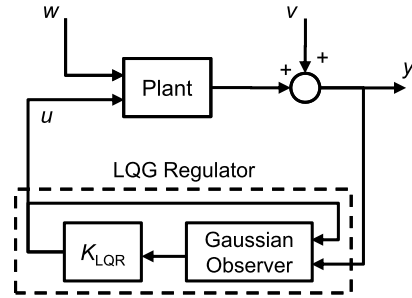
given noise covariance matrix. The structure of the LQG controller is illustrated in the closed-loop block diagram in Fig. 7.10. Same as with the original LQR controller, the Matlab function *lqg* in the Control System Toolbox finds the optimal LQG controller for a given LTI system as defined in Eqs. (7.20a), (7.20b). This function is employed in the design of the rotor lateral suspension controller for the compressor test rig.

7.3.2 Design of LQG Controller for Lateral Rotor Suspension

Here we discuss the design procedure of the AMB lateral suspension controller, which was implemented on the compressor surge test rig. An LQG controller was synthesized to optimize the closed-loop system based on the desired stability and performance criteria. Some of the optimized characteristics of the closed-loop system are the gain margin, the phase margin, the peak unbalance vibration, and the peak sensitivity function magnitude.

The final AMB plant equation modeled in Sect. 7.2 is a MIMO system, where the input is the commanded control signals to the AMB amplifiers, and the output is the sensor voltage signals corresponding to the measured rotor positions by the proximity sensors. For more information about the input and output of the AMB system, please refer to Sect. 7.2 on the modeling of the AMB radial suspension system. In order to simplify the design process of the LQG controller, we initially ignore the effects of the gyroscopics and only consider a single control axis for the combined motor-side (MS) and compressor-side (CS) radial bearings.

An iterative process is employed for the selection of the LQG weights that would produce the controller with the best performance and stability margin. During the minimization of the LQG cost function, the optimization problem is sensitive to the relative difference between the magnitudes of the penalty weights Q and R. This means that the absolute values of these weights are not as important as the ratio between the state and the input weights. Therefore, the design problem can be simplified by fixing the value of one penalty weight, and studying how the remaining weighting matrix affects the performance of the resulting LQG controller. In the design of the AMB suspension controller for the test rig, we selected the weighting

matrices to be

$$R = I, \tag{7.23}$$

$$Q = q_y C^{\mathrm{T}} C + q_i I, \tag{7.24}$$

where the constant q_y is the weight on the system output and q_i is the variable to iterate upon. Then, the LQG cost function becomes

$$J_{\mathrm{LQG}} = E\left\{ \lim_{T \to \infty} \int_0^T \left(q_y y^{\mathrm{T}} y + q_i x^{\mathrm{T}} x + u^{\mathrm{T}} u \right) \mathrm{d}t \right\}. \tag{7.25}$$

In this case, we observe from the above cost function that q_i is the penalty on the system states. This corresponds to the states of the sensor and amplifier models included in the AMB system, as well as the modal states of the free–free rotor. We recall here that the time constants of the amplifier and sensor models are small, and the state penalty in the LQG cost function will mostly depend on how fast the rotor states settle. Therefore, the weight q_i has an important effect on how much the rotor modes are excited during the AMB control, and how fast they are damped when excited by external disturbances.

The ratio of the output weight q_y to the state weight q_i was found to play an important role in the trade-off between robustness and performance of the AMB suspension system. Given a sufficiently large weight on the AMB system output, the controller will put most of its effort in keeping this output near zero by "clamping" the rotor at the measurement points. This will result in no direct attenuation of the internal vibrations of the rotor modes, which could eventually lead to instability of the AMB system. On the other hand, if the weight on the output is too small when compared to the state weight, then the closed-loop response with the resulting LQG controller will be sluggish in order to avoid the penalty of exciting the rotor modes. For our design, the rotor is considered to be rigid, thus a larger emphasis is put on regulating the system output. A reasonable value of q_y was found to be 0.2 for the state weight q_i ranging from 0.01 to 100. Additionally, we assume the noise level in both the control input and the feedback output signals to be 0.5 % of the signal full scale (FS) and the noise in each channel to be independent. This gives us a covariance matrix for the noise input of

$$W_{\mathrm{n}} = \begin{bmatrix} 2 \times 10^{-4} B^{\mathrm{T}} B & 0 \\ 0 & 2 \times 10^{-4} \end{bmatrix}. \tag{7.26}$$

During the iterative design process of the LQG controller that we present here, twenty values of q_i were selected between 0.01 and 100. For each iteration step in this process, the value of q_i is increased and the optimal LQG regulator minimizing the cost function J_{LQG} is computed. The relevant robustness and performance characteristics of the closed-loop AMB system with the derived controller were determined for each value of q_i. This information was collected, and then presented at the end of the iterative loop for all values of q_i's to select

the best state/output weight combination. Figure 7.11 demonstrates how the stability margins, the transient response, and the steady state characteristics of the LQG stabilized closed-loop system change as the state weight q_i is increased. The gain and phase margins are presented in Figs. 7.11(a) and 7.11(b), respectively, for the selected range of q_i. As the state weight is increased, a slight improvement in the stability margins can be initially observed due to the higher level of damping on the modes. However, as the value of q_i is further increased, both the gain and phase margins drop rapidly. The LQG controller becomes slow and sluggish due to the large penalty that results from exciting the rotor modal states.

A good transient response is generally required in an AMB system for a smooth transition between the different operating conditions of the rotating machine. Additionally, poor transient characteristics of the closed-loop system can be a warning flag for possible issues that could arise during the implementation of the feedback controller. The rise time, the settling time and the percentage overshoot corresponding to the step response at the motor-side and compressor-side AMBs are presented in Figs. 7.11(d), 7.11(e) and 7.11(f), respectively. As expected, both the rise time and the settling time tend to increase as the state weight increases and a larger penalty is given for exciting the rotor modes. By the same token, the overshoot of the step response decreases for the slower closed-loop system that results from increasing the value of q_i.

Two closed-loop characteristics in the ISO specifications that were monitored closely during design of the levitation controller are the peak magnitude of the sensitivity function and the peak vibration level in the unbalance response test. The change in these two values as a function of the state weight is presented in Fig. 7.12. The peak rotor displacement shown in Fig. 7.12(a) corresponds the forced response of the lateral suspension with an unbalance mass positioned at the rotor midspan. The size of the unbalance is selected to be $4U_b$, following the API 617 specification [6] for axial and centrifugal compressors as described in Chap. 2. The speed range in the unbalance response test is between zero and 30,000 rpm. The peak vibration level shown in Fig. 7.12(a) corresponds to the rotor maximum displacement at the system first critical speed Nc1. The peak displacement at this critical speed decreases as the damping on the system modes is increased together with the value of the state weight q_i. Based on the ISO 14839-2 standard, the vibration level of this machine is within the Zone A specification for all the values of q_i considered here.

The peak magnitude of the sensitivity function shown in Fig. 7.12(b) is also considered important in the design of the AMB suspension controller. The ISO 14839-3 standard discussed in Sect. 7.1 recommends a peak sensitivity value below 3 for new machines with AMBs. We observe from Fig. 7.12(b) that the closed-loop system with the LQG controller does not satisfy this requirement when the value of q_i is too large. This is in agreement with the drop in the gain margin observed in Fig. 7.11(a) for large values of q_i. The final value of the state weight was selected by considering all the trade-offs illustrated in Figs. 7.11 and 7.12. Stability margins, transient response and controller bandwidth were all considered in the selection of
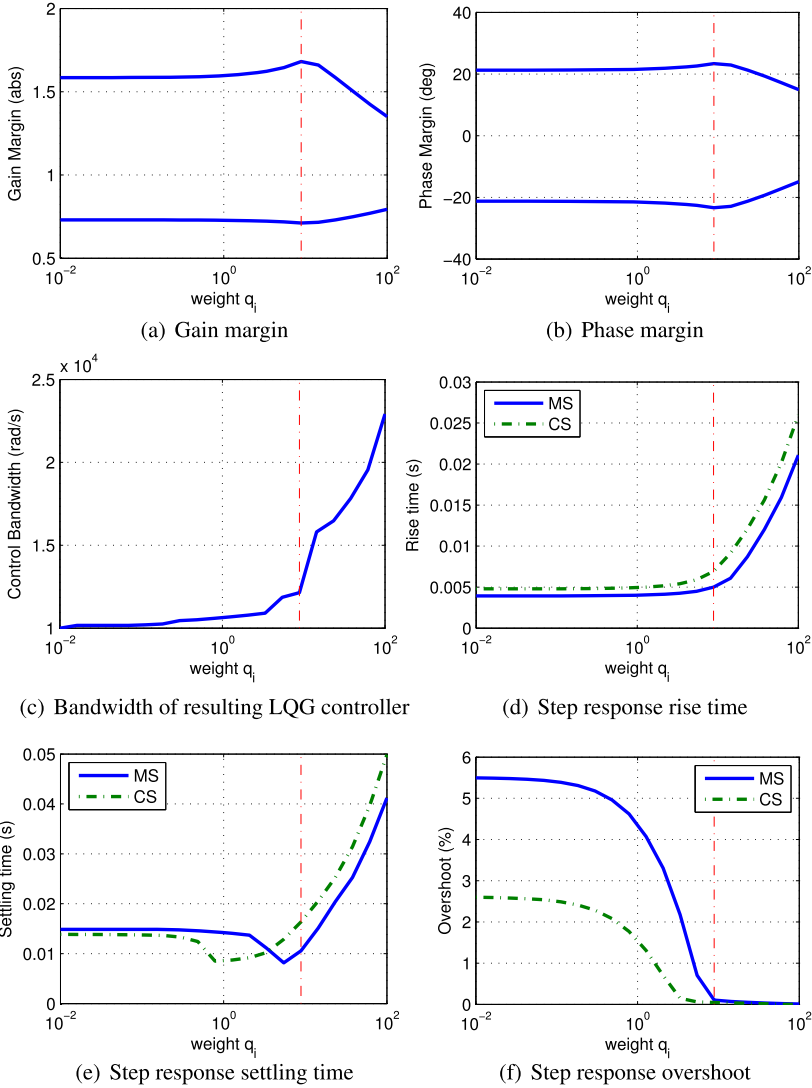
(a) Gain margin

(b) Phase margin

(c) Bandwidth of resulting LQG controller

(d) Step response rise time

(e) Step response settling time

(f) Step response overshoot

Fig. 7.11   Results from the design iteration of the LQG radial AMB suspension controller

the best value of q_i. In this case, the value $q_i = 8.9$ was decided to give the best stability margin of the closed-loop system and a reasonable controller bandwidth for digital implementation. The final value of q_i is marked in the above mentioned figures by a vertical dashed line.

The LQG controller corresponding to the selected state weigh q_i has a total of 24 states. The order of the controller is then reduced in Matlab by employing the Hankel singular value-based model reduction function *reduce* to 11. This reduction helps the implementation of the controller by eliminating unnecessary high-frequency com-

(a) Peak unbalance response vibration level   (b) Peak magnitude of the sensitivity function
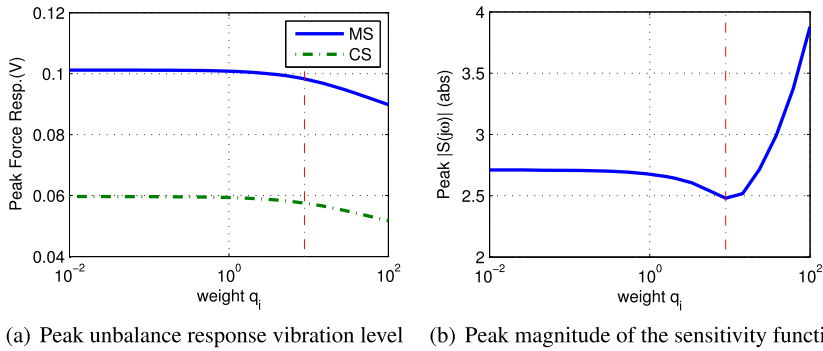
Fig. 7.12   ISO vibration and stability margin measures for the design iteration of the LQG radial AMB suspension controller
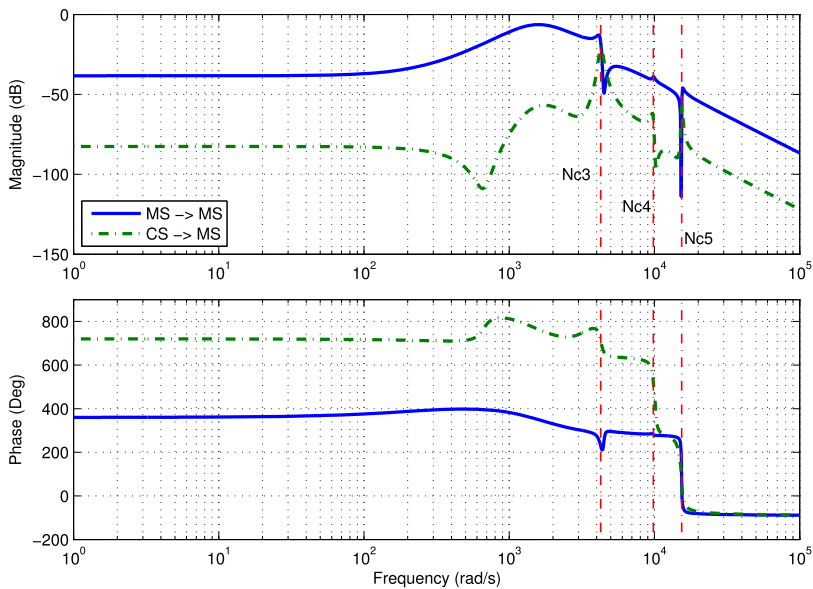

Fig. 7.13   Bode plots of the LQG controller at the motor-side (MS) output

ponents of the controller. The Bode plots of the final LQG controller are shown in Figs. 7.13 and 7.14, corresponding to the motor-side and the compressor-side control output, respectively. From these Bode plots, we can find some characteristics in the direct MS-to-MS and CS-to-CS parts of the LQG controller that are common in standard PID controllers for AMB systems. The constant gains at low/mid frequencies, the lead components at high frequencies, and the band-stop filters and phase bumps near the rotor critical speeds are all standard elements that are commonly found in elaborated PID controllers for AMB rotor suspension. In agreement
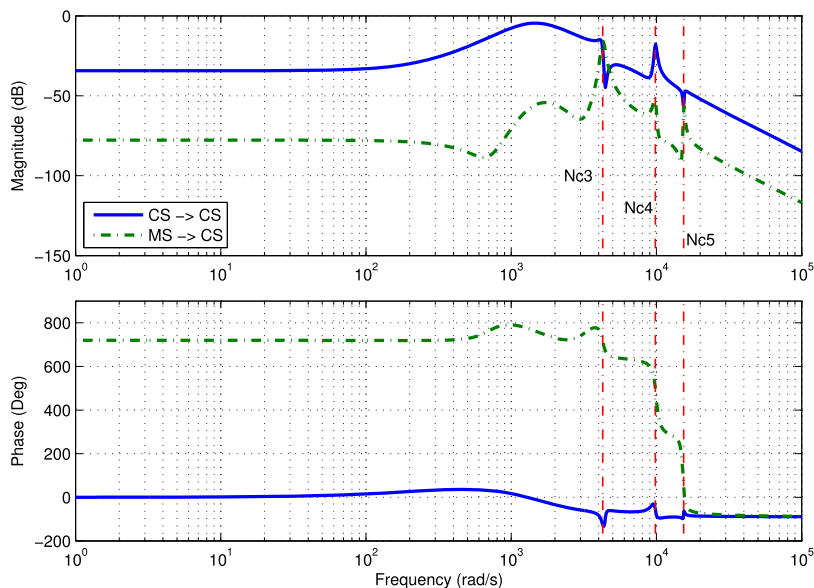
Fig. 7.14   Bode plots of the LQG controller at the compressor-side (CS) output

to the results presented in Fig. 7.11(c), the bandwidth of the final LQG controller is below 13,000 rad/s, and so the control algorithm is digitally implementable at the sampling rate specified by the hardware and software of the compressor test rig.

A simplified representation of the LQG-controlled system in terms of the closed-loop AMB stiffness can help to predict the location of the system critical speeds. The bearing stiffness is defined to be the reaction force f to a disturbance in the rotor position x, which can be simplified for one control axis of a single radial AMB as

$$F(s) = \left(K_i G_a(s)\left[K_{\mathrm{LQG}}(s)\right]_{1\times1} G_s(s) + K_x\right)X(s). \tag{7.27}$$

The transfer functions $G_a(s)$ and $G_s(s)$ represent the dynamics of the amplifier and sensor electronics, respectively. The controller equation $[K_{\mathrm{LQG}}(s)]_{1\times1}$ is here isolated to one axis of a single radial AMB by ignoring the cross-coupled terms between the bearings. Although stiffness in the traditional sense is a constant gain with no phase shift, the magnitude of Eq. (7.27) gives a close approximation of the AMB closed-loop stiffness at the low frequencies. The AMB stiffness curves for both the motor-side and the compressor-side AMBs are plotted on the critical speed map in Fig. 7.15. The crossings between the bearing stiffness and the critical speed curves give the predicted frequencies of the corresponding resonance modes. An advantage of Fig. 7.15 is that the simplified presentation of the controller in terms of closed-loop stiffness is more appealing for rotor-dynamic engineers in justifying the final locations of the critical speeds. Though not exact, the stiffness curve gives
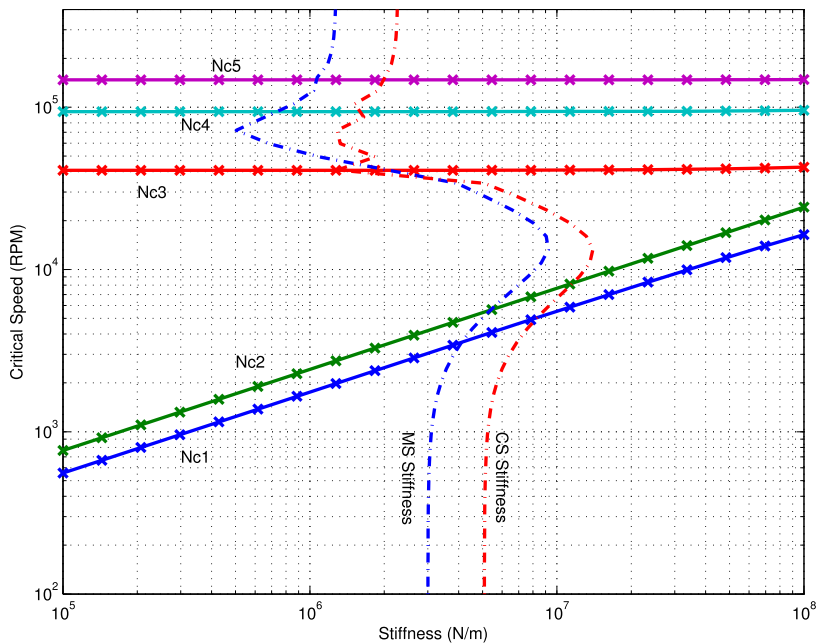
Fig. 7.15 Closed-loop AMB stiffness with the LQG controller

a starting point to introduce the different characteristics of the closed-loop levitation system.

The unbalance response of the radial AMB system is presented in Fig. 7.16 based on the mathematical model of the system and the final LQG controller. Two separate cases were simulated, following the specification in API 617 [6] on the size and location of the unbalance forces. The unbalance forces were located along the rotor length to excite the rotor modes within or near the speed range of the machine. Figure 7.16(a) shows the rotor vibrations for a single unbalance mass of $4U_b$ at the rotor midspan. In this case, the rotor parallel mode corresponding to Nc1 is excited in the forced response at the critical speed near 7,050 rpm. The maximum amplification factor (AF) for this mode combining the motor-side and compressor-side vibration levels is 0.72, and thus it is considered critically damped by the API standard. Also, the peak rotor displacement at the critical speed is below 30 % of the minimum clearance C_{min}, which would qualify the machine to Zone A as defined by the ISO 14839-2 standard.

The rotor vibration levels for unbalance masses of $4U_b$ located at each rotor end and separated by 180° in phase are shown in Fig. 7.16(b). In this case, the rotor conical mode is excited in the forced response, which corresponds to the critical speed Nc2 near 8,600 rpm. The maximum amplification factor (AF) for this mode combining the motor-side and compressor-side vibration levels is 0.82, which is once again within the range corresponding to critically damped modes as specified by the API standard. The peak rotor displacement at the critical speed in this case
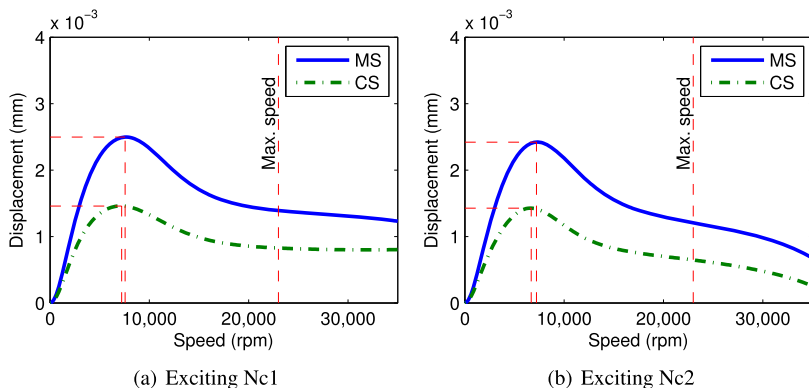
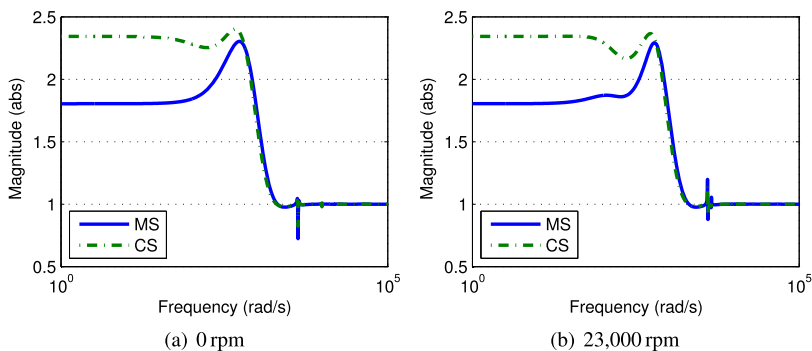Fig. 7.16 Simulated forced response with the unbalance mass as specified by API 617 [6]

Fig. 7.17 Magnitude of the sensitivity function at zero and the maximum continuous speed

is also below 30 % of the minimum clearance C_{min}, and the machine would again qualify for Zone A as defined by the ISO 14839-2 standard.

As introduced in Sect. 7.1, the ISO 14839-3 standard requires the magnitude of the sensitivity function to be below the maximum value of 3 to qualify for Zone A recommended for new machines with AMBs. The magnitude plots of the sensitivity function with the LQG controller is presented in Fig. 7.17 based on the mathematical model of the system. Because of the gyroscopic effects acting on the rotor, the dynamics of the closed-loop AMB system varies at different operating speeds of the compressor. Therefore, the sensitivity function is plotted in Fig. 7.17(a) at zero speed, and the same function is presented in Fig. 7.17(b) for the maximum design speed as specified by the ISO specification. In both cases, the peak magnitude is less than 3, which qualifies the machine for Zone A.

Finally, Table 7.3 summarizes the frequency and damping ratio corresponding to the resonance modes of the closed-loop radial AMB system, as well as the amplification factor from the forced response tests. Each mode is separated into the

Table 7.3 Rotor mode frequency and damping

Modes	Compressor 0 rpm		Compressor 23,000 rpm		AF
	Freq. (rad/s)	Damp. ratio	Freq. (rad/s)	Damp. ratio	
Nc1	−738	0.72	−640	0.49	0.72
	+738	0.72	+831	0.74	
Nc2	−902	0.73	−877	0.75	0.82
	+902	0.73	+970	0.71	
Nc3	−4,267	0.0056	−3,972	0.0021	
	+4,267	0.0056	+4,546	0.0011	
Nc4	−9,825	0.0015	−9,273	0.0012	
	+9,825	0.0015	+10,432	0.0011	
Nc5	−15,421	0.001	−14,678	0.001	
	+15,421	0.001	+16,273	0.001	

forward and the backward components, which are denoted by a "+" and a "−" sign, respectively. The frequency and damping ratio corresponding to each mode are presented for the static rotor and at the maximum design speed of 23,000 rpm. The table demonstrates that the first two modes of the system, which correspond to the rigid body dynamics of the rotor, are well damped. As for the higher frequency bending modes, the damping is marginally higher than the nominal modal damping added in the free–free rotor model. In a sense, these modes are far outside the speed range of the machine, and the best control strategy is to leave them undisturbed as much as possible.

7.3.3 Experimental Testing

In the experimental implementation of the LQG controller, a small integrator term was added to each control channel to compensate for static disturbances such as the rotor weight. The Bode plots of the radial AMB plant model derived in Sect. 7.2 are shown in Figs. 7.18 and 7.19 together with the measured plant frequency response from the experimental test rig. The Bode plots corresponding to a single control axis of the motor-side AMB are presented in Fig. 7.18, and the equivalent Bode plots for the compressor-side AMB are shown in Fig. 7.19. In these two cases, a good match is observed between the theoretical and the measured responses in both the magnitude and the phase curves. The experimental measurements clearly demonstrate that the rotor first bending mode Nc3 is accurately captured in the mathematical model.

A comparison between the theoretical and the measured Bode plots of the closed-loop sensitivity function is presented in Figs. 7.20 and 7.21 for the static rotor. In
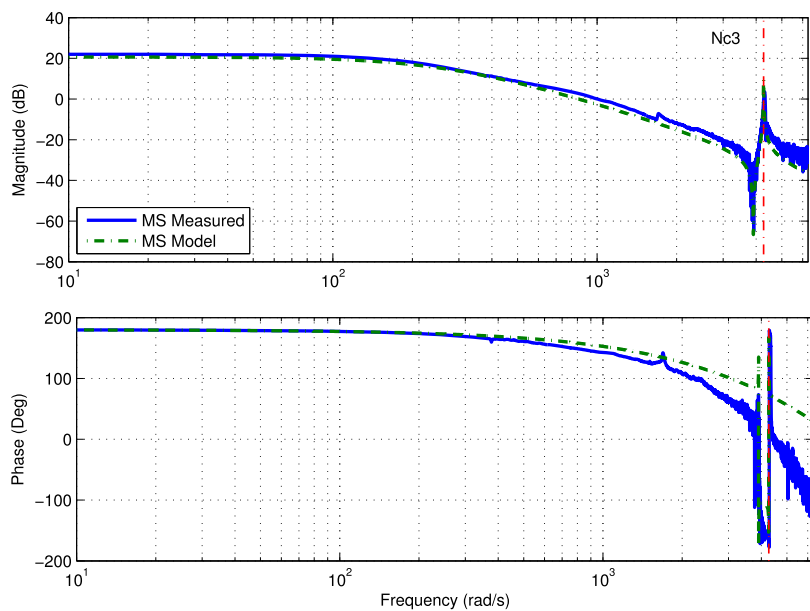
Fig. 7.18   Bode plots of the lateral AMB plant model at the motor side (MS)
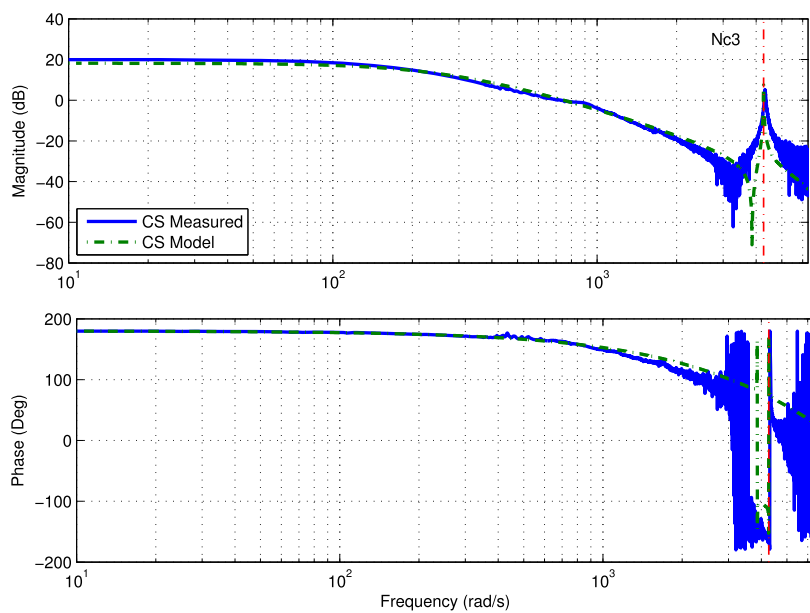

Fig. 7.19   Bode plots of the lateral AMB plant model at the compressor side (CS)
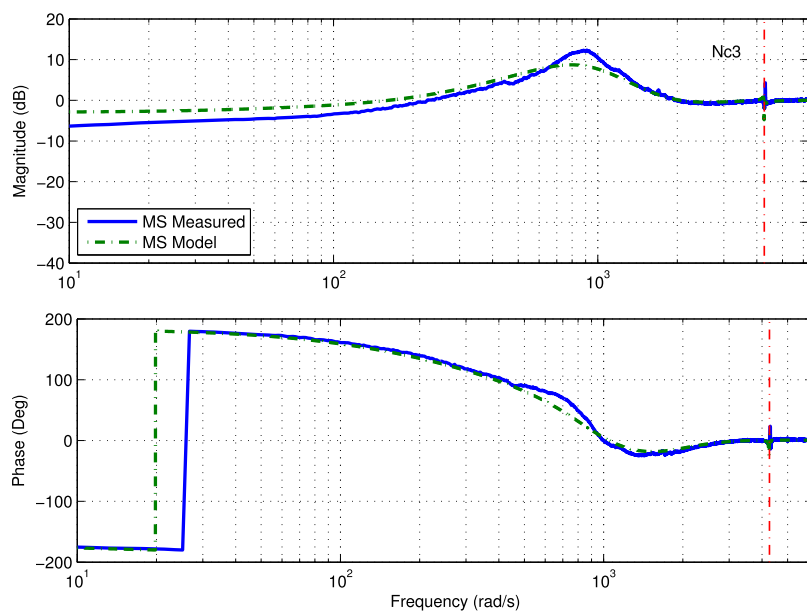
Fig. 7.20   Bode plots of the lateral AMB sensitivity function at the motor side (CS)
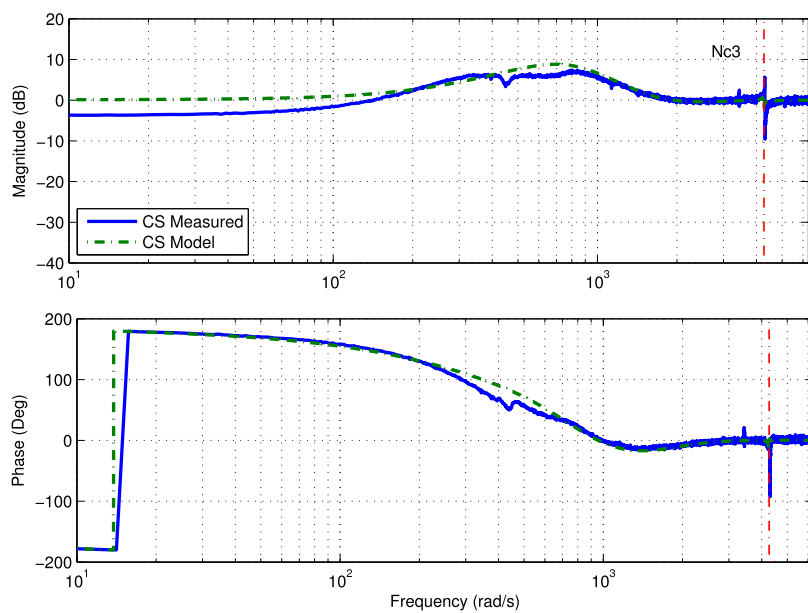

Fig. 7.21   Bode plots of the lateral AMB sensitivity function at the compressor side (CS)
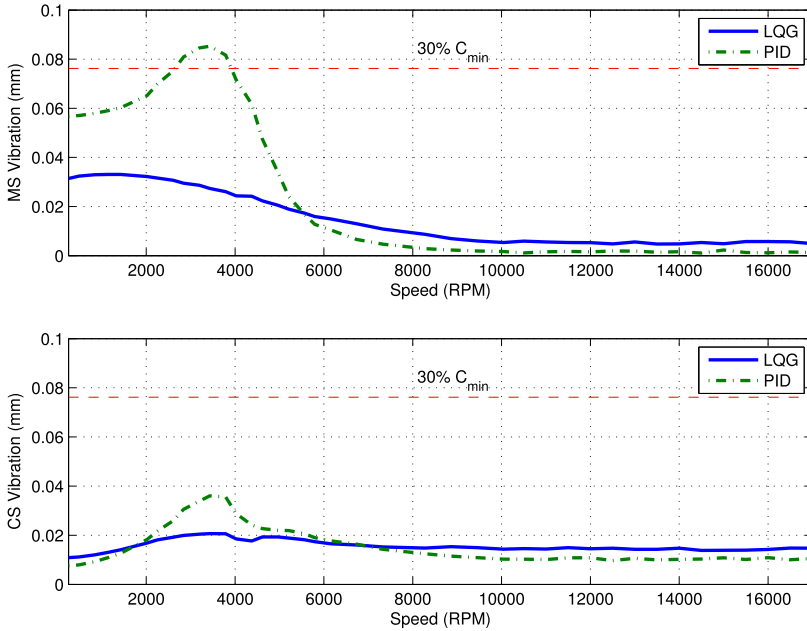
Fig. 7.22 Experimental rotor vibration level vs. speed

the same way as before, the Bode plots corresponding to a single control axis of
the motor-side AMB are presented in Fig. 7.20, and the equivalent Bode plots for
the compressor-side AMB are shown in Fig. 7.21. In both cases, a good match is
observed between the modeled and the actual system responses. Although the mea-
sured magnitude of the sensitivity function at the motor side was found to be slightly
above the mathematical prediction, surpassing the limit for Zone A as defined in
ISO 14839, it was concluded that the closed-loop system gives acceptable stability
margins for our testing purpose.

Finally, the measured rotor zero-to-peak vibration is shown in Fig. 7.22 for
the radial AMB suspension system. The rotor vibrations at the motor-side and the
compressor-side measurement points are recorded for the closed-loop system with
the final LQG controller. The same rotor vibrations are recorded for the AMB sys-
tem with a preliminary PID controller tuned for the initial levitation of the rotor.
Although these two controllers may not be appropriate for direct comparison since
the PID controller was only tuned for initial levitation, Fig. 7.22 clearly shows that
the LQG controller provides significant improvements from the original PID con-
troller in terms of rotor vibration. Particularly, it is seen that the vibration level at
the motor side with the PID controller exceeds the limit defined by ISO 14839 for
Zone A. On the other hand, the LQG controller maintains the rotor vibration well
within the recommended level for new machines with AMBs.

7.4 Control of Rotor Axial Dynamics

The design of the AMB suspension controller for the rotor axial dynamics is presented in this section. The controller is based on the thrust AMB model derived in Sect. 7.2. The axial AMB system is subjected to large aerodynamic disturbances acting on the compressor impeller, particularly during the surge instability. Additionally, the AMB surge controller requires accurate tracking of the rotor axial position to suppress the flow instability in the compression system. An H_∞ controller was designed for the axial AMB rotor support system to optimize the disturbance rejection and tracking capabilities for the closed-loop system. The many advantages of H_∞ controllers were discussed in Chap. 3 for AMB systems, and a general review of the theory was presented in Chap. 6.

7.4.1 Design of H_∞ Controller

In this section we present the design of an H_∞ controller for the stabilization of the thrust AMB dynamics. As discussed in Chap. 6, the H_∞ controller minimizes a cost function based on the infinity norm of the closed-loop system. Recall that the infinity norm, or the supremum norm, of a real rational proper transfer matrix $M(s)$ is defined as the supremum of the maximum singular value,

$$\left\| M(s) \right\|_\infty = \sup_{\omega \in \Re} \bar{\sigma}\left(M(j\omega) \right). \tag{7.28}$$

For the case when $M(s)$ describes the transfer function from the disturbance to the controlled output, the value of $\|M(s)\|_\infty$ measures the disturbance rejection capabilities of the system.

The design of the H_∞ controller is based on building an appropriate interconnected system $M(s)$, such that the design objectives of the closed-loop system can be written in the form of the inequality,

$$\left\| M(s) \right\|_\infty \leq 1. \tag{7.29}$$

Then, the objective of the H_∞ optimization problem is to find the stabilizing thrust controller $K_{th}(s)$ that minimizes the infinity norm of $M(s)$. If the minimizing controller satisfies the inequality in Eq. (7.29), then the desired closed-loop design objectives are achieved. Otherwise, the interconnected system is modified and the process is repeated. In the control of the thrust AMB in the compressor test rig, the principal design objective is to achieve good rotor tracking performance at the low and mid frequency range. This must be achieved while maintaining the controller bandwidth within the range limited by the digital implementation. Additionally, the closed-loop AMB system should have good capabilities of rejecting external disturbances entering the system.
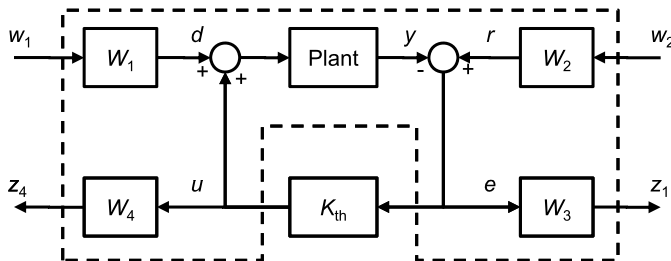
Fig. 7.23 Interconnected system for the design of the thrust AMB rotor support controller

7.4.2 Design of H_∞ Controller for Axial Rotor Support

Consider the interconnected system in Fig. 7.23, where the proper and stable weighting transfer functions $W_i(s)$'s are defined arbitrarily. The weighted input of the interconnected system is w_1 and w_2, which correspond to the input disturbance signal d and the reference rotor position r, respectively. On the other end, the output of the interconnected system is z_1 and z_2, which are the weighted signals of the control input u and the rotor position error e. Finally, the stabilizing thrust controller closing the loop in Fig. 7.23 is represented by $K_{th}(s)$. The input/output system equations of the interconnected system is found to be

$$\begin{bmatrix} z_1 \\ z_2 \end{bmatrix} = \begin{bmatrix} -W_3 S_{th} G_{th} W_1 & W_3 S_{th} W_2 \\ -W_4 T_{th} W_1 & W_4 S_{th} K_{th} W_2 \end{bmatrix} \begin{bmatrix} w_1 \\ w_2 \end{bmatrix}, \qquad (7.30)$$

where G_{th} is the thrust AMB plant model derived in Sect. 7.2, and S_{th} and T_{th} are the sensitivity and the complementary sensitivity functions of the closed-loop AMB system, respectively. Recall from Chap. 6 that these closed-loop transfer functions are defined as

$$S_{th} = \frac{1}{1 + G_{th} K_{th}},$$

and

$$T_{th} = \frac{G_{th} K_{th}}{1 + G_{th} K_{th}}.$$

Looking at the interconnected system in Eq. (7.30), we notice that many of the design requirements for the thrust AMB are captured in the equations between the w_i's and the z_i's. The tracking error of the rotor axial position can be lowered by reducing the magnitude of $S_{th}(s)$, which appears in the equations for the interconnected system between the weighting functions $W_2(s)$ and $W_3(s)$. At the same time, the control effort in the thrust AMB to a reference input signal is lowered by reducing the magnitude of $S_{th}(s)K_{th}(s)$, which also appears in Eq. (7.30) together with the weighting functions $W_2(s)$ and $W_4(s)$. The remaining transfer functions in

Eq. (7.30) represent the transmission of the input disturbance to the control output in $S_{\text{th}}(s)G_{\text{th}}(s)$ and the closed-loop thrust AMB dynamics from the reference to the actual rotor position in $T_{\text{th}}(s)$.

Based on the input/output equations of the interconnected system, the appropriate weighting functions were selected so that the control objectives are stated in the form of Eq. (7.29). For example, the combined magnitude of the weights $W_2(s)$ and $W_3(s)$ acting on the sensitivity function was selected to have large values at the low/mid frequencies. This forces the magnitude of $S_{\text{th}}(s)$ down in the same frequency range in order to make the total magnitude of $M(s)$ less than one. On the other hand, the combined weight acting on the transfer function $S_{\text{th}}(s)K_{\text{th}}(s)$ has a large magnitude at high frequencies, which eventually limits the bandwidth of the final H_∞ controller. Higher penalties on the control effort force the magnitude of the controller to start rolling off at lower frequencies. The trade-off between the two design objectives discussed above results from the fact that the magnitude of the sensitivity function cannot be small at both the low/mid- and the high-frequency ranges [46]. Therefore, in selecting the weighting functions, we have to keep in mind the limited capabilities of the AMB system. For the thrust AMB in the compressor test rig, the final weights for the synthesis of the H_∞ controller were chosen to be

$$W_1(s) = 0.07, \tag{7.31a}$$

$$W_2(s) = 1, \tag{7.31b}$$

$$W_3(s) = 100\frac{0.0015s + 1}{0.5s + 1}, \tag{7.31c}$$

$$W_4(s) = 0.01\frac{(10^{-3}s + 1)^2}{(10^{-5}s + 1)^2}. \tag{7.31d}$$

The magnitudes of the combined weighting functions are plotted in Fig. 7.24 as they appear in the interconnected system in Eq. (7.30).

The final H_∞ controller was synthesized with the weighting functions as given in Eqs. (7.31a)–(7.31d). The derived thrust AMB controller has a total number of 13 states, which is the same as the combined number of states for the weighting functions and the plant model. The Bode plots in Fig. 7.25 show that the structure of the controller is relatively simple, with a large magnitude at the low-frequency range, a large phase lead at the mid-frequency range, and a fast drop in magnitude at the higher frequencies. The bandwidth of the controller is about 3,000 rad/s, which is digitally implementable with the available hardware and software in the experimental test rig.

The magnitudes of the transfer functions in the interconnected system in Eq. (7.30) are plotted in Fig. 7.26 with the synthesized controller for the thrust AMB. We observe that the magnitudes of the interconnected system between the weighted input and the weighted output are below the upper bound of one for all frequencies. Therefore, the design objectives identified for the H_∞ synthesis are satisfied by the derived controller. Also, the trade-off between the different

(a) From w_1 to z_1

(b) From w_2 to z_1

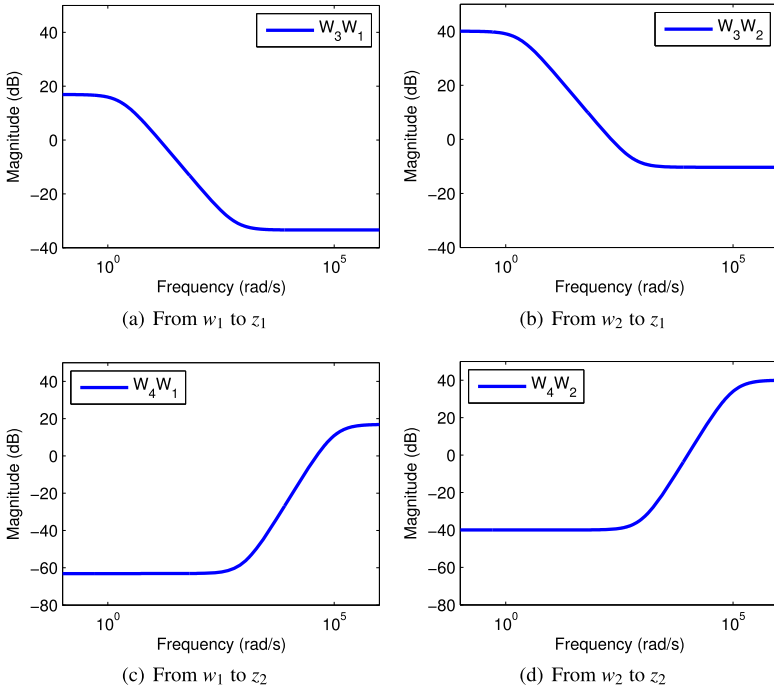(c) From w_1 to z_2

(d) From w_2 to z_2

Fig. 7.24 Magnitude of the weighting functions between the input and output channels of the interconnected system in Eq. (7.30)
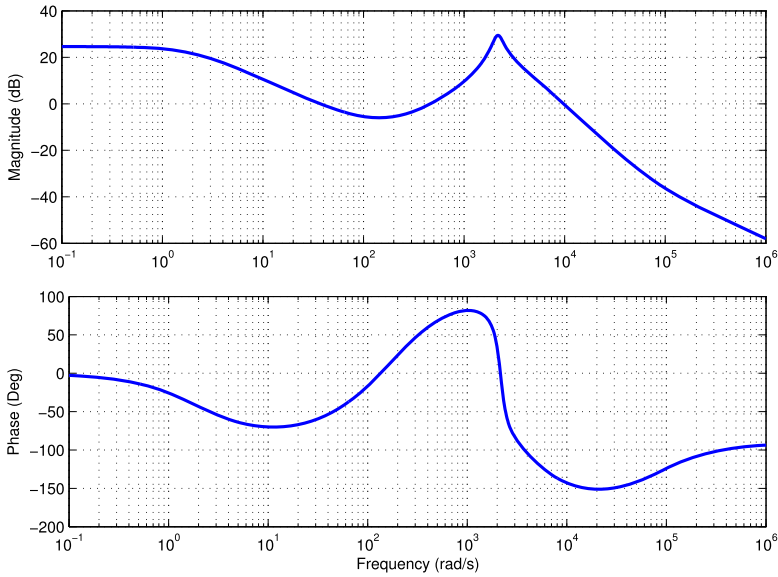

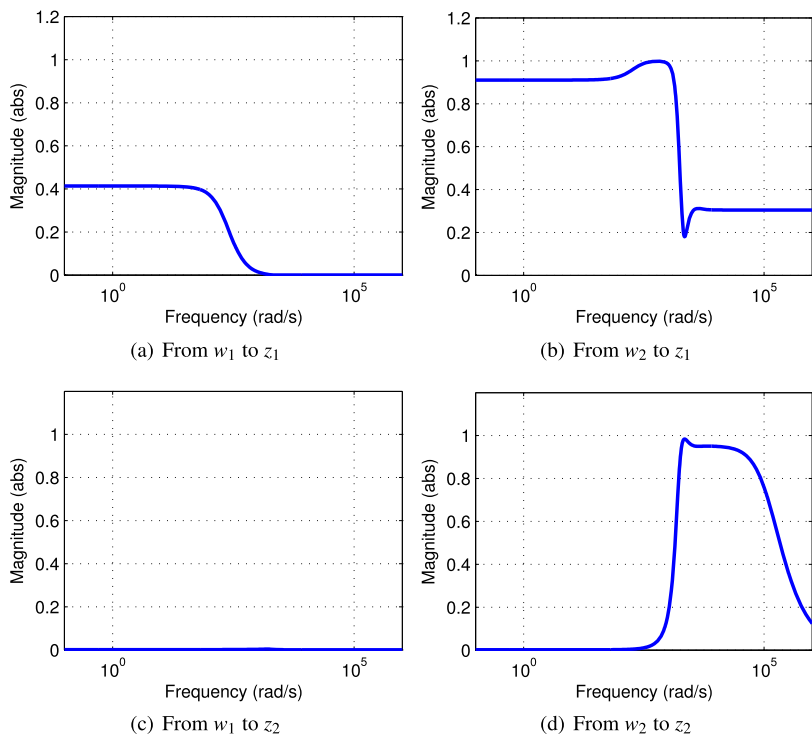**Fig. 7.25** Bode plots of the final thrust AMB controller

(a) From w_1 to z_1

(b) From w_2 to z_1

(c) From w_1 to z_2

(d) From w_2 to z_2

Fig. 7.26   Magnitude of the interconnected system in Eq. (7.30) with final H_∞ controller

design requirements defined in the H_∞ optimization problem can be observed
clearly in Fig. 7.26. The requirement in the tracking performance is represented
in Fig. 7.26(b), and the constraint in the control effort is given in Fig. 7.26(d).
We observe in these figures that the input and output weights were selected so
that they do not penalize the magnitude of the two design requirements at the
same frequency range. This corresponds to the obvious limitation that good track-
ing of the rotor position requires a large control effort by the AMB, and simi-
larly a small control effort by the AMB will result in poor rotor tracking perfor-
mance.

   Finally, the Bode plots of the sensitivity function $S_{th}(s)$ and the complementary
sensitivity function $T_{th}(s)$ are presented in Fig. 7.27 based on the modeled closed-
loop thrust AMB equations. The magnitude of the sensitivity function is kept small
at low frequencies to achieve a good tracking performance. The zero-crossover fre-
quency of $|S_{th}(j\omega)|$ is near 200 rad/s. Also, the peak value of the magnitude is
below 9.5 dB as recommended by the ISO 14839-3 standard for new machines with
AMBs. The magnitude of the complementary sensitivity function indicates that,
with the synthesized H_∞ controller, the closed-loop bandwidth of the thrust AMB
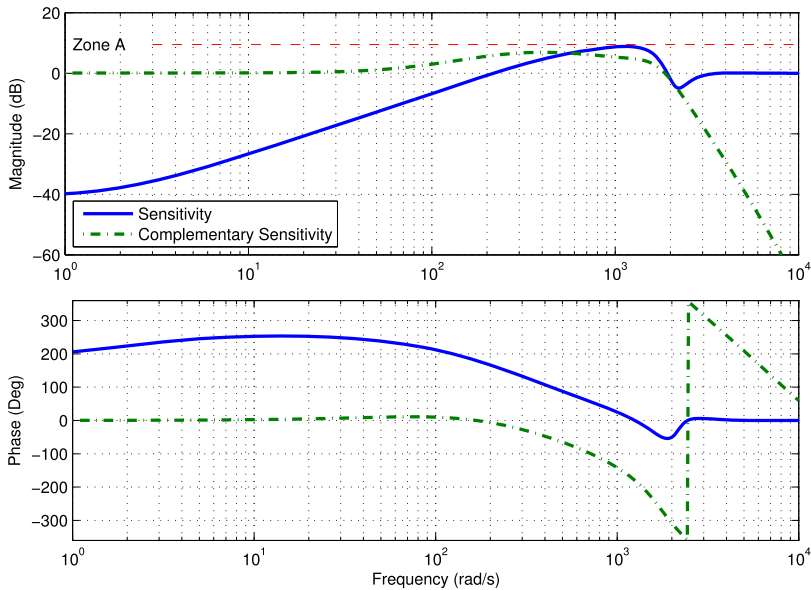system is approximately 2,000 rad/s.

Fig. 7.27 Bode plots of the thrust AMB sensitivity and complementary sensitivity functions

7.4.3 Experimental Testing

Same with the radial AMB levitation controller, a small integrator term is added in the experimental implementation of the thrust AMB controller to compensate for the static disturbances affecting the rotor in the axial direction. The measured Bode plots of the open-loop transfer function in the absence of the controller are presented in Fig. 7.28 together with the modeled system response. These Bode plots were measured for frequencies up to 4,000 rad/s. Good agreement in both the magnitude and phase plots is found between the theoretical and experimental responses.

The measured and theoretical Bode plots of the sensitivity function are presented in Fig. 7.29. The measured and model-based curves match well in both the magnitude and the phase plots. At low frequencies, both measured and simulated Bode plots have low magnitudes, which indicate good rotor tracking performance by the closed-loop system. The measured peak magnitude of the sensitivity is below 9.5 dB, in agreement with the theoretical prediction. This peak magnitude satisfies the requirement for Zone A in the ISO 14839-3 specification for new machines with AMBs.

Finally, the measured and the model-based Bode plots of the complementary sensitivity function are shown in Fig. 7.30. Once again, the magnitude and the phase plots corresponding to the experimental response are well matched by the model-based Bode plots. The measured bandwidth of the closed-loop thrust AMB system is around 2,000 rad/s, which also agrees with the corresponding theoretical prediction.
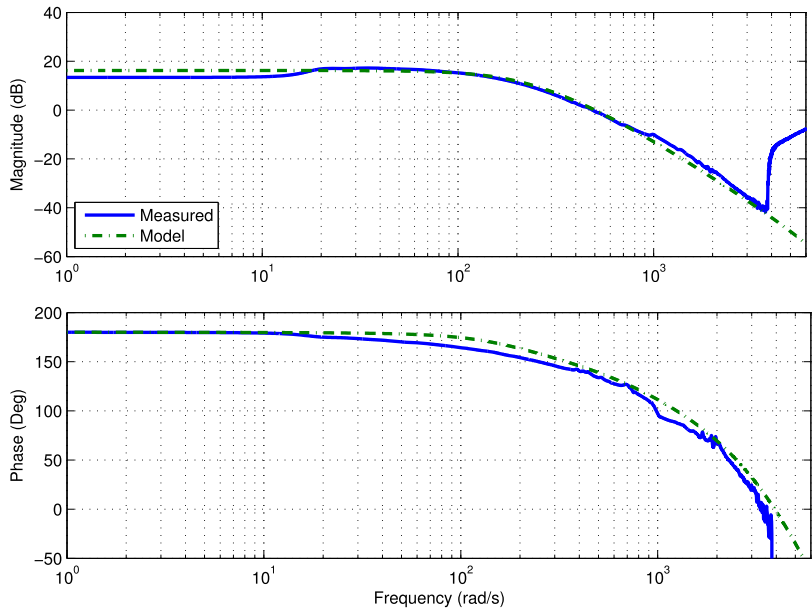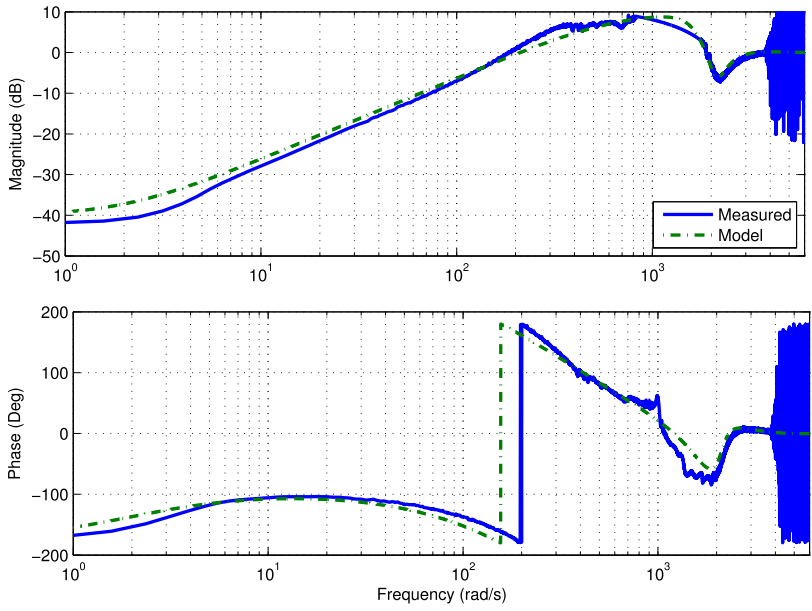
Fig. 7.28 Bode plots of the axial AMB plant model

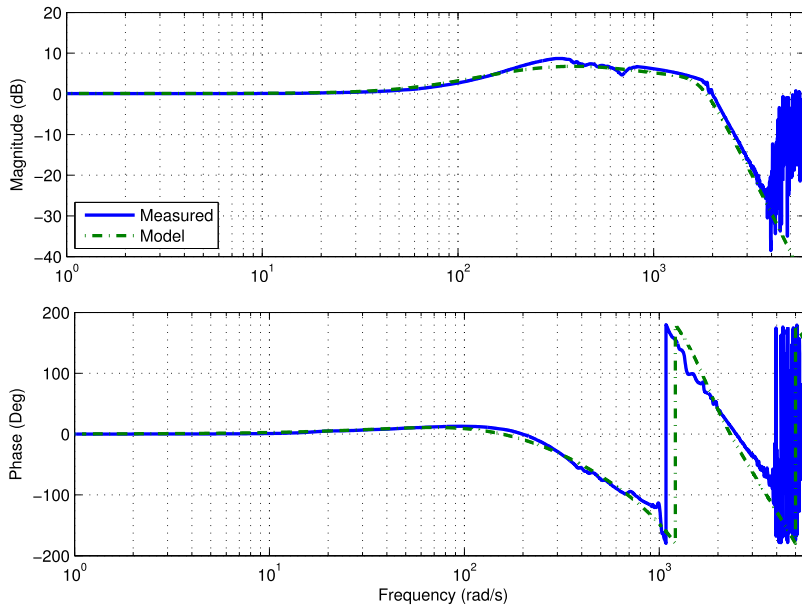**Fig. 7.29** Bode plots of the axial AMB sensitivity function

Fig. 7.30 Bode plots of the axial AMB complementary sensitivity function

7.5 Conclusions

The design of the rotor levitation controllers for the AMBs in the compressor test rig was presented in this chapter. First of all, the standards that define the requirements and recommendations for rotating machines with AMBs were discussed. The system recommendations found in the ISO 14839 standards for new machines were listed in the chapter. These recommendations were employed throughout this chapter as guidelines for the design of the AMB levitation controllers in the compressor test rig. Next, the equations describing the lateral and axial dynamics of the rotor/AMB systems were derived. A detailed model of the rotor, the AMB actuator and all major electronic components were obtained. Some bearing losses such as eddy currents and back-EMF effects were also included in the final model.

Finally, the rotor levitation controllers were designed for the compressor test rig, based on the derived models of the AMB system dynamics. The controllers were designed to satisfy the recommendations in the standards discussed earlier in this chapter. The lateral position of the rotor was regulated by LQG controllers designed to minimize the vibration due to the unbalance forces. In the axial direction, an H_∞ controller was designed to optimize the rotor axial tracking performance. The designed AMB controllers were implemented on the compressor test rig, and experimental measurements were presented to validate the theoretical design. The measured responses of the closed-loop AMB systems demonstrated satisfactory results for both the axial and the radial bearings.